JMEPEG (2025) 34:13037–13043
https://doi.org/10.1007/s11665-025-11225-2

©The Author(s)
1059-9495/$19.00

ORIGINAL RESEARCH ARTICLE

Grain Refinement and Solute Distribution in Zircaloy-4 Following High-Pressure Torsion

Siyu Huang, Levi Tegg, Sima Aminorroaya Yamini, Zhiyang Wang, Yi Huang, Limei Yang, Ondrej Muránsky, Ingrid McCarroll, Patrick A. Burr, and Julie M. Cairney

Submitted: 14 October 2024 / Revised: 20 November 2024 / Accepted: 15 December 2024 / Published online: 25 April 2025

Zirconium (Zr) alloys, such as Zircaloy-4, are widely used for structural components and fuel cladding in industrial nuclear fission applications. High-pressure torsion (HPT), a severe plastic deformation process, produces an ultra-fine grain structure with properties that may have benefits in the nuclear industry, but the microstructural implications of processing of Zr alloys using this technique have not yet been extensively explored. Here, electron microscopy and atom probe tomography were used to investigate the microstructure and solute distribution in an as-received Zircaloy-4 and a fine-grained HPT-processed sample. Fe segregates to grain boundaries in both samples, however, at much lower concentrations after HPT processing, indicating that Fe diffuses to the newly formed grain boundaries during the severe plastic deformation. Although Sn segregates to the grain boundaries of the as-received sample, it is distributed almost homogenously in the HPT-processed sample, which may provide advantages for corrosion resistance. Very low concentrations of Cr alloying elements at the matrix and grain boundaries of both samples are attributed to precipitation.

Keywords atom probe tomography, high-pressure torsion, solute segregation, Zircaloy-4

1. Introduction

Zirconium (Zr) alloys are used for structural components and fuel cladding in the core of nuclear reactors because of their low neutron absorption cross section and high corrosion resistance (Ref 1). It has long been recognized that, in contrast to other metal alloys, the corrosion performance of zirconium alloys deteriorates with the increase in their purity and very small variations in alloying elements or microstructure significantly change corrosion resistance and mechanical properties of these alloys (Ref 2). High-pressure torsion (HPT) is a severe plastic deformation method that subjects a thin disk-shaped sample to concurrent high pressure and torsional stress (Ref 3), resulting in grain refinement and potential phase transformations in many alloy systems (Ref 4, 5). HPT can reduce grain sizes in Zr alloys to $\sim$ 100 nm with high uniformity and stability (Ref 6, 7), and is being explored as a method to produce alloys with improved properties as a result of their unique structure. During service in reactors, Zr alloys experience a neutron flux that causes irradiation-induced damage, as well as high thermal and mechanical stresses that can lead to component deformation or failure. HPT introduces defects in the microstructure, including a very high density of grain boundaries (Ref 4, 8, 9), which may act as sinks for the irradiation-induced point defects. Therefore, it is thought that HPT can potentially enhance the tolerance to the irradiation damage of Zr alloys in service.

Metastable ω-Zr and β-Zr phases have been reported to form during HPT processing of Zr alloys (Ref 6, 7, 10, 11). Similar grain structures were observed in Ti alloys that underwent severe plastic deformation, indicating that this could be a characteristic shared by materials with hexagonal close-packed (hcp) structures that have been treated at a low strain rate and ambient temperature (Ref 11). The evolution of grains in severely deformed Zr alloys has been previously studied (Ref 4, 5, 8, 12); however, the effect of this severe plastic deformation on the distribution of alloying elements, which are detrimental to corrosion performance of Zr alloys, has not been studied. Understanding the distribution of solutes in Zr alloys between the matrix grains and boundaries is crucial for managing their in-reactor corrosion behavior (Ref 13). Here, the evolution of the microstructure and the distribution of solute atoms in an as-received plate of Zircaloy-4 is compared with the same alloy that has been processed by HPT, by using

Siyu Huang, Levi Tegg, Sima Aminorroaya Yamini, and **Julie M. Cairney**, Australian Centre for Microscopy and Microanalysis, The University of Sydney, Sydney 2006, Australia; and School of Aerospace, Mechanical and Mechatronic Engineering, The University of Sydney, Sydney 2006, Australia; **Zhiyang Wang** and **Ondrej Muránsky**, Australian Nuclear Science and Technology Organisation (ANSTO), Sydney 2232, Australia; and School of Mechanical Engineering, University of New South Wales, Sydney 2052, Australia; **Yi Huang**, Department of Design and Engineering, Faculty of Science and Technology, Bournemouth University, Poole, Dorset BH12 5BB, UK; and Materials Research Group, Department of Mechanical Engineering, University of Southampton, Southampton SO17 1BJ, UK; **Limei Yang**, Department of Design and Engineering, Faculty of Science and Technology, Bournemouth University, Poole, Dorset BH12 5BB, UK; and School of Civil & Environmental Engineering, University of Technology Sydney, Sydney 2007, Australia; **Ingrid McCarroll**, Max-Planck-Institut für Eisenforschung, Max-Planck-Str. 1, 40237 Düsseldorf, Germany; and **Patrick A. Burr**, School of Mechanical Engineering, University of New South Wales, Sydney 2052, Australia. Contact e-mail: julie.cairney@sydney.edu.au.

electron back-scatter diffraction (EBSD), transmission Kikuchi diffraction (TKD), and atom probe tomography (APT).

2. Materials and Methods

The as-received (hot-rolled and annealed) Zircaloy-4 plate has a chemical composition of Zr-0.82 Sn-0.26 Fe−0.11 Cr-0.15 O-0.003 N and H- $<$ 0.01 Ni, Mo, Nb, Co, Pd, Ru, V, and Al (wt.%), measured by inductively coupled plasma atomic emission spectroscopy (ICP-AES). A disk of 10 mm diameter and 0.8 mm thickness was prepared, oriented with the flat surfaces aligned to the original rolling direction. HPT was performed under 6.0 GPa pressure at room temperature, with 10 revolutions at a rate of 1 rpm (designated as N10 in previous work (Ref 8)). Both samples were electropolished at room temperature using an electrolyte of 95% methanol and 5% perchloric acid at 30 V DC for EBSD analysis, performed by a Zeiss UltraPlus Scanning Electron Microscope. The as-received sample was sectioned into matchsticks and sharpened into sharp needles using two stages of electropolishing by conventional methods (Ref 14). The electropolished needles were transferred to a Thermofisher G4 Hydra plasma focused ion beam (FIB) for annular milling and TKD analysis, in order to position a grain boundary near the specimen apex (Ref 15). The HPT-processed specimens were prepared by the standard FIB lift-out and annular milling (Ref 16). HPT-processed specimens were extracted from midway along the radius of the sample to avoid microstructural irregularities at the center or periphery of the disk (Ref 8, 17). TKD patterns of both samples were collected using an Oxford Instruments EBSD system using a 30-kV beam voltage. Patterns were analyzed using Oxford Instruments HKL Tango software, where data was cleaned for wild spikes and four nearest neighbors. APT was performed using a Cameca LEAP4000X Si at a base temperature of 50 K, using pulse frequency of 200 kHz, a target detection rate of 0.5%, and laser pulse energy of 100 pJ, similar to previous studies (Ref 18-20). Data was reconstructed and analyzed using Cameca's Visualization and Analysis Software (AP Suite 6). The average evaporation field was set for Zr (28 V/nm), and the detector efficiency was 0.57. The AP Suite 6 default image compression factor 1.65 and k-factor 3.3 were used, as no poles were observed, and post-evaporation images were not collected to calibrate the reconstruction.

3. Results and Discussion

Figure 1 shows the EBSD results from both the (a) as-received and (b) HPT-processed Zircaloy-4 samples, showing the inverse pole figure plot (IPF X) (note the scale difference). The grain sizes in the as-received sample range from 1 to 45 μm. The HPT-processed sample composed of predominantly nano-sized grains (~27 nm). Detailed EBSD analysis of these samples is reported elsewhere (Ref 8).

Figure 2 shows the site-specific FIB-milled specimens of the two specimens after annular milling, and correlated TKD data, used to locate grain boundaries prior to the APT experiment. Figure 2(a) and (e) shows scanning electron microscopy (SEM) images of the tips from the as-received and HPT samples, respectively, with the red boxes indicating the area analyzed

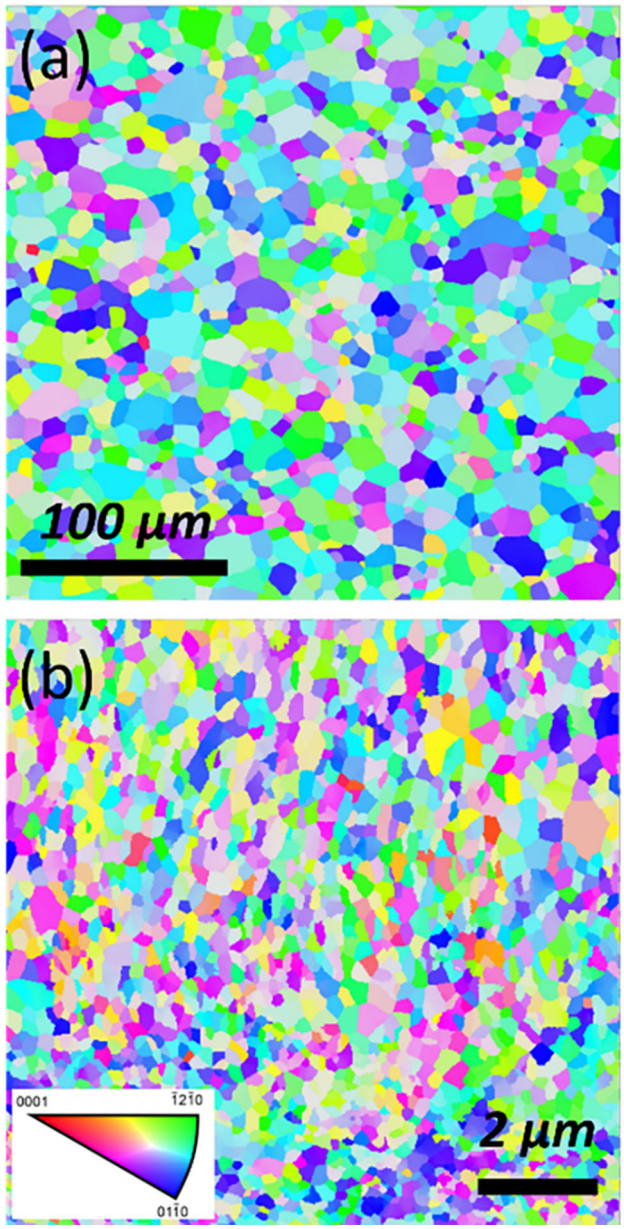


Fig. 1 EBSD inverse pole figure (IPF X) orientation maps of the (a) as-received; and (b) HPT-processed samples, indicating significant reduction in grain size of the sample following HPT processing

with TKD. Figure 2(b) to (d) shows the band contrast (BC) map, inverse pole figure (IPF) Y, and IPF Z of the region of interest, respectively, for the as-received sample. The grain boundary sits approximately 100 nm below the apex of the tip. Figure 2(f) to (h) shows the BC map, IPF Y, and IPF Z data, respectively, for the HPT sample. Grain sizes at the apex of the HPT specimen vary from 30 to 100 nm, consistent with the EBSD results presented in Figure 1. Only α-Zr was detected in the mapping area. Previous reports noted that ω-Zr, which formed during HPT processing, reverted to α-Zr during TEM sample preparation by FIB milling (Ref 8). The same milling method has been used in our study to prepare the APT tips and no evidence of ω-Zr phase was observed in the TKD, confirming the transformation of the metastable phase to α-Zr.

Figure 3(a) shows an APT reconstructed volume showing the solute element positions (Fe, Al, Sn, Cr, and Si) from the as-received sample (Fig. 2a). A grain boundary is visible on the left and is enriched with Fe, Al, and Cr, while Si appears to be randomly distributed. Si and Al are residual elements likely introduced to this alloy from raw materials used during casting.

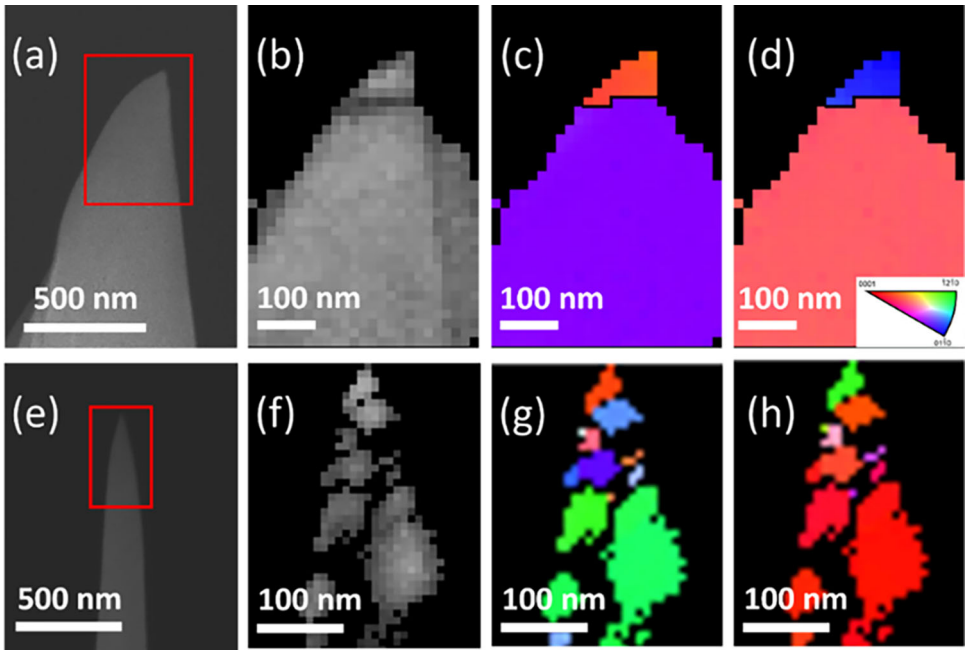


Fig. 2 The SEM image and TKD results of as-received Zircaloy-4 sample: (a) SEM image, (b) BC map, (c) IPF Y, and (d) IPF Z; and HPT-processed sample: (e) SEM image, (f) BC map, (g) IPF Y, (h) IPF Z, following site-specific FIB milling

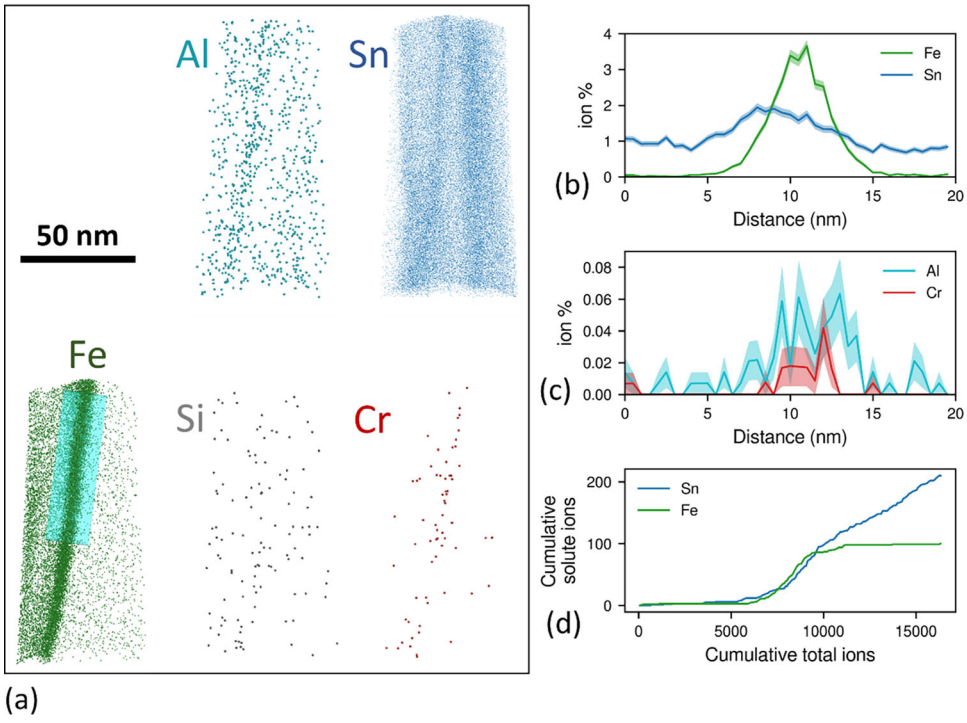


Fig. 3 (a) APT reconstruction of the tip shown in Fig. 2(a) from the as-received sample, the position of ROI to calculate the interfacial excess of solute atoms is shown in Fe reconstruction. *Al, Cr, Si, and Fe are rendered with spheres to enhance visibility. All reconstructed species are shown at the same magnification and from the same viewing angle;* (b) concentration variation of Fe and Sn in the ROI shown in (a); (c) concentration variation of Al and Cr in the ROI shown in (a), the shaded area around the curves refers to the uncertainty of calculated values of concentrations, the composition analysis was performed in the direction normal to the grain boundary; (d) cumulative profiles of Fe and Sn atoms detected across the grain boundary

A region of interest (ROI) of 65 nm × 15 nm × 20 nm was created (Fig. 3a) to calculate a compositional profile normal to the grain boundary. Figure 3(b) and (c) shows one-dimensional composition profiles of Fe, Sn, and Cr, Al. Fe is nearly absent in the α-Zr grains; however, its concentration increases at the grain boundary to ∼ 3.5 at.%. Sn is dissolved in the Zr matrix with a concentration of ∼ 1.0 at.%, increasing to ∼ 2 at.% near the grain boundary. There are also regions of higher Sn concentrations that extend along the z direction in the dataset due to field-enhanced migration of Sn during APT analysis of the tip, causing artifacts in the reconstruction (Ref 18, 19). Al and Cr show maximum concentrations of ∼ 0.03 at.% and 0.2 at.% at the grain boundary, respectively.

Care needs to be taken in interpretation of these compositions, especially the maximum measured concentration, as the boundary may not be perfectly perpendicular to the ROI, it may not be completely flat, and differences in evaporation field may result in trajectory aberrations. To quantify Fe and Sn segregation more accurately, cumulative compositional profiles were calculated from multiple smaller ROIs, normal to the grain boundary. An example cumulative profile of Fe and Sn from one of these ROI is shown in Fig. 3(d). The average Gibbsian interfacial excess (Γ_i) (Ref 20) for Fe and Sn at this grain boundary from these multiple ROIs is calculated to be $\Gamma_{Fe} = 0.52 \pm 0.04$ monolayers and $\Gamma_{Sn} = 0.28 \pm 0.18$ monolayers.

Figure 4 shows the APT reconstruction of the tip prepared from the HPT-processed sample (Fig. 2e) for Fe, Al, Cr, Si, Cu, and Sn. As for the as-received sample, Fe segregates to grain boundaries which are observed in the lower half of the reconstruction. The grain boundaries are annotated in Fig. 4 to guide the eye. The data contains a grain boundary triple junction, and the three grain boundaries are labeled 'GB 1,' 'GB 2,' and 'GB 3.'

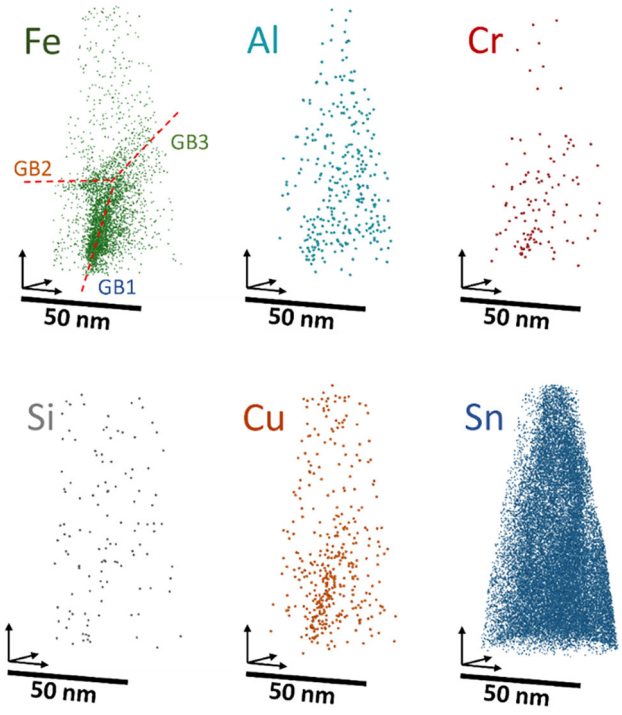


Fig. 4 APT reconstruction of the tip shown in Figure 2(a) for the HPT-processed sample, presenting distribution of Fe, Al, Cr, Si, Cu, and Sn in the tip. All elements are rendered with spheres to enhance visibility

Figure 4 shows the segregation of Cu to the boundaries. This element was not detected in the as-received sample. Cu, Si, and Al are residual elements in this alloy and therefore their random distribution within the sample is expected.

Three cylindrical ROIs (10 nm diameter and 20 nm height) were positioned normal to each grain boundary to measure the composition of solute atoms at the boundary. Figure 5(a) shows the variation in concentration of Fe, Sn, Cr, and Al across three grain boundaries. Similar to the as-received sample, Fe is nearly absent in the α-Zr matrix, but is enriched at the three grain boundaries, reaching peak concentrations of ∼ 1.8 at.% at GB 1, ∼ 0.9 at.% at GB 2, and ∼ 0.5 at.% at GB 3. The concentration of Sn does not vary significantly between the matrix and grain boundaries, which is consistent with the ion distribution shown in Fig. 5. Al shows no measurable enrichment at grain boundaries. Due to the very low number of Cr and Al atoms detected at the grain boundaries, the relative uncertainty of the measured values is high. This analysis indicates that residual atoms of Al, Si, and Cu are present at very low concentrations in this alloy and distributed randomly within the grain and grain boundaries of the HPT-processed sample. Concentrations of these elements are too low to have

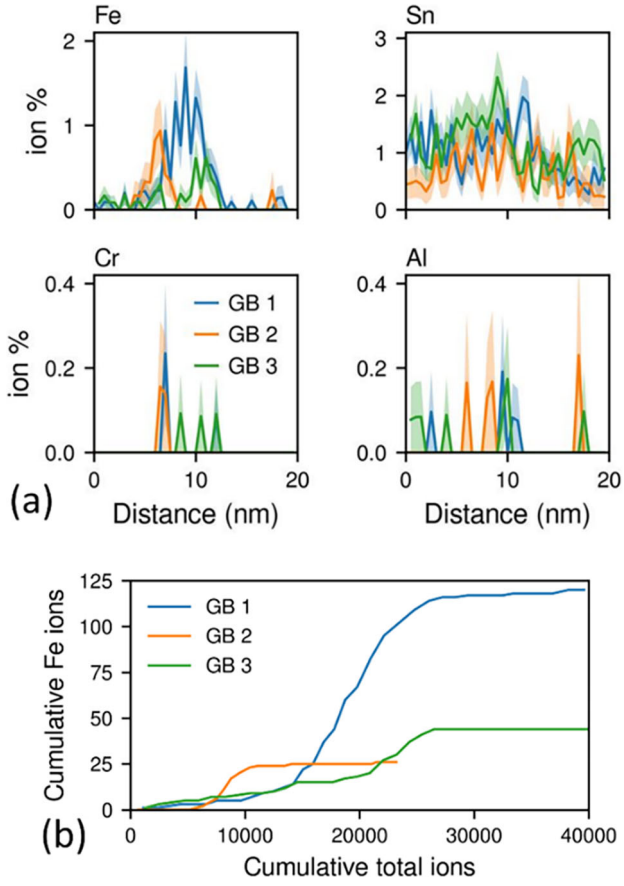


Fig. 5 (a) 1D concentration profiles of elements across the ROI normal to the grain boundaries shown in fig. 5 for Fe, Sn, Cr, and Al. The shaded regions around the lines represent uncertainties of the analysis; (b) Example cumulative profiles of Fe atoms detected across the grain boundaries (GB 1, 2, and 3) in the HPT-processed sample. Cuboid regions with equal cross section crossed both grains perpendicular to the interfaces

meaningful segregation analysis. The Gibbsian interfacial excess of the Fe was calculated from cumulative compositional profiles determined for three smaller cylindrical ROIs (with cross section 10 nm × 10 nm) for GB1, GB2, and GB3, all normal to the grain boundaries. Figure 5(b) shows example cumulative profiles of Fe atoms detected across the three grain boundaries. Γ_{Fe} values at the different grain boundaries are $\Gamma_{Fe}(GB1) = 3.4 \pm 3.2$ atoms/nm^2, $\Gamma_{Fe}(GB2) = 0.73 \pm 0.65$ atoms/nm^2, and $\Gamma_{Fe}(GB3) = 1.4 \pm 0.7$ atoms/nm^2. The uncertainty provided is the difference between the average of the three cylindrical ROIs and the measured value which is most different. The Γ_{Fe} for the as-received sample was 5.7 ± 0.4 atoms/nm^2 monolayers, which is much higher than for the HPT-processed sample, suggesting redistribution of Fe during the severe plastic deformation.

The alloying element Sn in Zircaloy-4 can dissolve in the Zr matrix, while Fe and Cr are predominantly found in the $Zr(Cr,Fe)_2$ Laves precipitates (Ref 21). The low concentration of Fe observed in the matrix (0.022 at.%) in the as-received sample is consistent with the Zr-Fe phase diagram (Ref 22). This alloy has undergone hot rolling and stress-relief annealing, resulting in an exceptionally low content of Fe in α-Zr (Ref 23). Fe has previously been detected at grain boundaries in Zr alloys (Ref 21, 24-27). Similarly, our results indicate that Fe can segregate to the grain boundaries at concentrations higher than the equilibrium Fe solubility (120 wt ppm at 800 °C and less than 50 wt ppm < 300 °C (Ref 22)) in the α-Zr matrix without forming precipitates (Fig. 3 and 5). However, the HPT-processed sample contains less Fe segregation at grain boundaries than the as-received sample. We have analyzed grain boundaries in several atom probe specimens for both the as-received and HPT-processed samples, in which the concentration of Fe at grain boundaries of HPT-processed specimens was consistently lower than the ones in as-received sample. Specimens reported here are examples of data collected from these samples to avoid repetition.

The Fe at the newly generated grain boundaries can only originate from the original grain boundaries or from second phase particles (mostly Laves phase). A previous synchrotron x-ray diffraction study (Ref 8) of Zircaloy-4 showed no significant changes in the peak intensities of second phase particles (SPPs) after the HPT processing, suggesting that the dissolution of SPPs does not occur during HPT. The decrease in concentration of Fe at the grain boundaries following HPT is therefore attributed to the redistribution of Fe from the original boundaries throughout the newly formed interfaces and dislocation sites. Strain-induced diffusion of alloying elements occurs in severely deformed metals (Ref 28, 29), where solute atoms are carried by defects such as dislocations while increased concentration of vacancies during severe plastic deformation also enhances the atomic mobility.

As a qualitative approximation, in dilute alloy systems, high-angle grain boundaries have been shown to have greater levels of solute segregation than low-angle boundaries (Ref 30, 31), though the temperature and presence of other solutes in a multicomponent system strongly affect the solute enrichment factor at the grain boundaries (Ref 30). The three grain boundaries we analyzed in the HPT-processed sample exhibit differing concentrations of solutes (Fig. 5a) and the differences are most dramatic for Fe. HPT processing has increased the surface area of grain boundaries significantly (Fig. 1). Several high- and low-angle grain boundaries are observed within 200 nm of the atom probe tip prepared from the HPT-processed sample (Fig. 2f to h). The much higher concentration of Fe at GB1 relative to GB2 and GB3 is thought to be due to differences in the nature of the boundaries, where GB1 is likely to be a high-angle boundary, and the other two boundaries are thought to be low-angle boundaries.

Despite a low concentration of Cr in both the matrix and the grain boundaries, Cr enrichment was visible in both samples (Fig. 3c and 5c). This alloy nominally contains 0.11 wt.% Cr, half of the nominal composition of Fe. The tendency of solute segregation is inversely related to its bulk solubility (Ref 30). Segregation of Cr to grain boundaries is reported in quenched sample of binary Zr-0.15 wt.% Cr alloy (Ref 27) and Zr-Fe-Cr alloys (Ref 32). The Cr concentration is too low for a meaningful segregation quantification, as the measured difference is within the range of uncertainty. Previous work (Ref 27) also noted the formation of spherical particles by Cr at the grain boundaries of a quenched sample (referred to as segregation); these might be nuclei of precipitates if the sample was further annealed. The regions we analyzed contained much more Fe than Cr (much more than double), suggesting that the Cr in this alloy is mostly consumed by Cr-rich precipitates, such as the $Zr(Fe,Cr)_2$ Laves phase (Ref 33).

Interestingly, Sn clearly segregates to the grain boundaries of the as-received Zircaloy-4 but appears homogenously distributed in the HPT-processed sample. Lower Sn segregation at the grain boundaries benefits the strength of the alloy (Ref 34), so Sn segregation to grain boundaries in Zr alloys has been extensively studied (Ref 21, 25, 34-36), but findings are inconsistent. Some studies argue that Sn segregation observed at grain boundaries is related to the known artifacts linked to the field-enhanced migration of Sn (Ref 18, 19). We do not believe that is the case here, as the boundary lies at an angle to the long axis of the reconstruction and can be observed separately to the field-induced migration. Sn segregation has not been observed in ZIRLO (Ref 26); however, studies report Sn segregation at the grain boundaries of Zircaloy-2 (Ref 35), Zircaloy-4 (Ref 21), and CZ1 (Ref 25). Grain boundary segregation of Sn was not evident in the HPT sample, but variations in the Sn concentration can be seen across the dataset (Fig. 5), so field-induced migration may be clouding the observations. The very small grain sizes and highly distorted structure of the matrix from severe deformation probably also affect the migration of Sn during field evaporation. So, while we observe that severe deformation reduces Sn segregation (potentially advantageous for mechanical properties), further work is required to confirm this effect.

In general, we have observed the segregation of Fe, Cr, Al, and Sn in the as-received Zy-4 with their reduced concentrations at the grain boundaries in the HPT-processed sample. Previous studies (Ref 37, 38) have introduced a so-called effective temperature in the HPT-processed metals that refers to an elevated temperature at the phase diagram in which the same concentration of solutes observed at HPT-processed metal analyzed at the room temperature. This implies that the severe plastic deformation of metals results in the formation of supersaturated solid solutions (Ref 38, 39). According to the binary phase diagrams, the solubilities of Fe, Al, Sn, and Cr are limited in α-Zr at room temperature while these solubility limits increased significantly by temperature. It is likely that effective temperature for this HPT-processed sample is much higher than the room temperature, similar to previous studies (Ref 37, 39); therefore, the solute elements can potentially diffuse back to the Zr matrix which dissolves higher concentrations of solutes at

the effective temperature than the room temperature. This can alternatively explain the reduction in concentrations of segregated solute elements to grain boundaries in the HPT-processed sample.

4. Conclusions

In summary, Zircaloy-4 forms ultra-fine grains after the HPT processing. Fe, Cr, and Al segregate at the grain boundaries in both as-received and HPT-processed samples. Sn is segregated to the grain boundary in the as-received sample, but we did not find such clear evidence of segregation in HPT-processed samples. Cr segregates at boundaries but is only observed at very low concentrations. This element has extremely low solubility in Zr alloys and is thought to be consumed to form precipitates. Residual elements of Si and Cu were detected in some grains and grain boundaries. The concentration of Fe at grain boundaries of the as-received sample is much higher than that of HPT-processed sample due to the increase in available grain boundary area in the HPT sample to accommodate Fe atoms. Fe concentration varies considerably between grain boundaries in the HPT-processed sample, most likely due to different grain boundary structures (low-angle vs higher-angle boundaries).

Acknowledgments

This work was supported by the Australian Research Council (ARC) grants FT180100232 and IM230100125. The authors acknowledge the technical and scientific support provided by Sydney Microscopy and Microanalysis at the University of Sydney, and the support of Microscopy Australia.

Funding

Open Access funding enabled and organized by CAUL and its Member Institutions.

Conflict of interest

On behalf of all authors, the corresponding author states that there is no conflict of interest.

Open Access

This article is licensed under a Creative Commons Attribution 4.0 International License, which permits use, sharing, adaptation, distribution and reproduction in any medium or format, as long as you give appropriate credit to the original author(s) and the source, provide a link to the Creative Commons licence, and indicate if changes were made. The images or other third party material in this article are included in the article's Creative Commons licence, unless indicated otherwise in a credit line to the material. If material is not included in the article's Creative Commons licence and your intended use is not permitted by statutory regulation or exceeds the permitted use, you will need to obtain permission directly from the copyright holder. To view a copy of this licence, visit http://creativecommons.org/licenses/by/4.0/.

References

1. A.T. Motta, L. Capolungo, L.Q. Chen, M.N. Cinbiz, M.R. Daymond, D.A. Koss, E. Lacroix, G. Pastore, P.C.A. Simon, and M.R. Tonks, Hydrogen in Zirconium Alloys: A Review, *J. Nucl. Mater.*, 2019, **518**, p 440–460
2. A.T. Motta, A. Couet, and R.J. Comstock, Corrosion of Zirconium Alloys Used for Nuclear Fuel Cladding, *Annu. Rev. Mater. Res.*, 2015, **45**, p 311–343
3. N. Smirnova, V. Levit, V. Pilyugin, R. Kuznetsov, L. Davydova, and V. Sazonova, Evolution of the Structure of fcc Single Crystal Subjected to Strong Plastic Deformation, *Fiz. Metal. Metalloved*, 1986, **61**(6), p 1170
4. Z. Yu, S. Jin, M. Feng, M.Y. Murashkin, R.Z. Valiev, S.P. Ringer, and G. Sha, Temperature-Dependent-Composition of η Phase in an Al-Zn-Mg-Cu Alloy under High Pressure Torsion: Kinetics and Thermodynamics, *Acta Mater.*, 2022, **237**, 118181
5. M. Stückler, H. Krenn, P. Kürnsteiner, B. Gault, F. De Geuser, L. Weissitsch, S. Wurster, R. Pippan, and A. Bachmaier, Intermixing of Fe and Cu on the Atomic Scale by High-Pressure Torsion as Revealed by DC-and AC-SQUID Susceptometry and Atom Probe Tomography, *Acta Mater.*, 2020, **196**, p 210–219
6. M.T. Pérez-Prado, A. Gimazov, O.A. Ruano, M. Kassner, and A. Zhilyaev, Bulk Nanocrystalline ω-Zr by High-Pressure Torsion, *Scripta Mater.*, 2008, **58**(3), p 219–222
7. Y. Wang, M. Louie, Y. Cao, X. Liao, H. Li, S. Ringer, and Y. Zhu, High-Pressure Torsion Induced Microstructural Evolution in a Hexagonal Close-Packed Zr Alloy, *Scripta Mater.*, 2010, **62**(4), p 214–217
8. L. Chen, Z. Wang, H. Zhu, P.A. Burr, J. Qu, Y. Huang, L. Balogh, M. Preuss, and O. Muránsky, On the Microstructure and High-Temperature Stability of Nano-Grained Zircaloy-4, *Scripta Mater.*, 2022, **210**, 114410
9. R. Harsha, V.M. Kulkarni, and B.S. Babu, Severe Plastic Deformation-a Review, *Mater. Today: Proc.*, 2018, **5**(10), p 22340–22349
10. A.P. Zhilyaev, A.V. Sharafutdinov, and M.T. Pérez-Prado, Phase Transformations During High-Pressure Torsion of Pure Zr and of a Zr-2.5% Nb Alloy, *Adv. Eng. Mater.*, 2010, **12**(8), p 754–757
11. R. Haraguchi, Y. Yoshimatsu, T. Nagaoka, M. Arita, K. Edalati, and Z. Horita, Electrical Resistivity Mapping of Titanium and Zirconium Discs Processed by High-Pressure Torsion for Homogeneity and Phase Transformation Evaluation, *J. Mater. Sci.*, 2017, **52**, p 6778–6788
12. X. Sauvage, G. Wilde, S. Divinski, Z. Horita, and R. Valiev, Grain Boundaries in Ultrafine Grained Materials Processed by Severe Plastic Deformation and Related Phenomena, *Mater. Sci. Eng. A*, 2012, **540**, p 1–12
13. B. Cox, Some Thoughts on the Mechanisms of In-Reactor Corrosion of Zirconium Alloys, *J. Nucl. Mater.*, 2005, **336**(2–3), p 331–368
14. B. Gault, M.P. Moody, J.M. Cairney, and S.P. Ringer, Atom Probe Microscopy, Springer Science & Business Media, 2012
15. K. Babinsky, R. De Kloe, H. Clemens, and S. Primig, A Novel Approach for Site-Specific Atom Probe Specimen Preparation by Focused ion Beam and Transmission Electron Backscatter Diffraction, *Ultramicroscopy*, 2014, **144**, p 9–18
16. M.K. Miller and K.F. Russell, Atom Probe Specimen Preparation with a Dual Beam SEM/FIB Miller, *Ultramicroscopy*, 2007, **107**(9), p 761–766
17. X. An, S. Wu, Z. Zhang, R. Figueiredo, N. Gao, and T. Langdon, Evolution of Microstructural Homogeneity in Copper Processed by High-Pressure Torsion, *Scripta Mater.*, 2010, **63**(5), p 560–563
18. J. Wei, P. Frankel, E. Polatidis, M. Blat, A. Ambard, R. Comstock, L. Hallstadius, D. Hudson, G. Smith, and C. Grovenor, The Effect of Sn on Autoclave Corrosion Performance and Corrosion Mechanisms in Zr-Sn-Nb Alloys, *Acta Mater.*, 2013, **61**(11), p 4200–4214
19. D. Hudson, A. Cerezo, and G.D. Smith, Zirconium Oxidation on the Atomic Scale, *Ultramicroscopy*, 2009, **109**(5), p 667–671
20. M.K. Miller, Atom Probe Tomography: Analysis at the Atomic Level, Springer Science & Business Media, 2012
21. Y. Dong, A.T. Motta, and E.A. Marquis, Atom Probe Tomography Study of Alloying Element Distributions in Zr Alloys and their Oxides, *J. Nucl. Mater.*, 2013, **442**(1–3), p 270–281

22. C.-C. Wei, A. Aitkaliyeva, Z. Luo, A. Ewh, Y.H. Sohn, J.R. Kennedy, B.H. Sencer, M.T. Myers, M. Martin, J. Wallace, M.J. General, and L. Shao, Understanding the Phase Equilibrium and Irradiation Effects in Fe-Zr Diffusion Couples, *J. Nucl. Mater.*, 2013, **432**(1), p 205–211
23. H. Zou, G. Hood, J. Roy, R. Schultz, and J. Jackman, The Solid Solubility of Fe in α-Zr: a Secondary ion Mass Spectrometry Study, *J. Nucl. Mater.*, 1994, **210**(3), p 239–243
24. J. Eriksson, G. Sundell, P. Tejland, H.-O. Andrén, and M. Thuvander, Nanoscale Chemistry of Zircaloy-2 Exposed to Three and Nine Annual Cycles of Boiling Water Reactor Operation—an Atom Probe Tomography Study, *J. Nucl. Mater.*, 2022, **561**, 153537
25. W. Lin, Q. Lv, D. Jiao, L. Zhang, J. Tan, G. Sha, and J. Hu, Creep-Induced Redistribution of Alloying Elements in CZ1 Zirconium Alloys, *J. Mater. Sci. Tech.*, 2024, **173**, p 31–44
26. D. Hudson and G.D. Smith, Initial Observation of Grain Boundary Solute Segregation in a Zirconium Alloy (ZIRLO) by Three-Dimensional Atom Probe, *Scripta Mater.*, 2009, **61**(4), p 411–414
27. B. Gault, P.J. Felfer, M. Ivermark, H. Bergqvist, J.M. Cairney, and S.P. Ringer, Atom Probe Microscopy Characterization of as Quenched Zr-0.8 wt% Fe and Zr–0.15 wt% Cr Binary Alloys, *Mater. Lett.*, 2013, **91**, p 63–66
28. X. Sauvage, A. Duchaussoy, and G. Zaher, Strain Induced Segregations in Severely Deformed Materials, *Mater. Trans.*, 2019, **60**(7), p 1151–1158
29. G. Wilde and S. Divinski, Grain Boundaries and Diffusion Phenomena in Severely Deformed Materials, *Mater. Trans.*, 2019, **60**(7), p 1302–1315
30. S. Hofmann and P. Leiĉek, Solute Segregation at Grain Boundaries, *Interface Sci.*, 1996, **3**(4), p 241–267
31. X. Zhou, X.-X. Yu, T. Kaub, R.L. Martens, and G.B. Thompson, Grain Boundary Specific Segregation in Nanocrystalline Fe(Cr), *Sci. Rep.*, 2016, **6**(1), p 34642
32. P.A. Burr, M.R. Wenman, B. Gault, M.P. Moody, M. Ivermark, M.J.D. Rushton, M. Preuss, L. Edwards, and R.W. Grimes, From Solid Solution to Cluster Formation of Fe and Cr in α-Zr, *J. Nucl. Mater.*, 2015, **467**, p 320–331
33. A.W. Aldeen, Z.W. Chen, I.A. Disher, M. Samiuddin, and K. Yan, Second Phase Particles in Zr-Sn-Nb-Fe Alloys: A Review, *Phys. Metals Metallography*, 2023, **124**(4), p 362–379
34. Z. Xue, X. Zhang, J. Qin, M. Ma, and R. Liu, Exploring the Effects of Solute Segregation on the Strength of Zr {1011−1} Grain Boundary: A First-Principles Study, *J. Alloy. Compd.*, 2020, **812**, 152153
35. T. Sawabe and T. Sonoda, Evolution of Nanoscopic Iron Clusters in Irradiated Zirconium Alloys with Different Iron Contents, *J. Nucl. Sci. Technol.*, 2018, **55**(10), p 1110–1118
36. R. Yuan, Y.-P. Xie, T. Li, C.-H. Xu, M.-Y. Yao, J.-X. Xu, H.-B. Guo, and B.-X. Zhou, An Origin of Corrosion Resistance Changes of Zr Alloys: Effects of Sn and Nb on Grain Boundary Strength of Surface Oxide, *Acta Mater.*, 2021, **209**, 116804
37. A. Mazilkin, B. Straumal, A. Kilmametov, P. Straumal, and B. Baretzky, Phase Transformations Induced by Severe Plastic Deformation, *Mater. Trans.*, 2019, **60**(8), p 1489–1499
38. B.B. Straumal, S.G. Protasova, A.A. Mazilkin, E. Rabkin, D. Goll, G. Schütz, B. Baretzky, and R.Z. Valiev, Deformation-Driven Formation of Equilibrium Phases in the Cu-Ni Alloys, *J. Mater. Sci.*, 2012, **47**(1), p 360–367
39. B.B. Straumal, A.S. Gornakova, A.A. Mazilkin, O.B. Fabrichnaya, M.J. Kriegel, B. Baretzky, J.Z. Jiang, and S.V. Dobatkin, Phase Transformations in the Severely Plastically Deformed Zr-Nb Alloys, *Mater. Lett.*, 2012, **81**, p 225–228

Publisher's Note Springer Nature remains neutral with regard to jurisdictional claims in published maps and institutional affiliations.